nature catalysis

ARTICLES

https://doi.org/10.1038/s41929-020-0476-3

Molecular-level insights on the reactive facet of carbon nitride single crystals photocatalysing overall water splitting

Lihua Lin[1,2], Zhiyou Lin[1], Jian Zhang[1], Xu Cai[1], Wei Lin[1], Zhiyang Yu[1] and Xinchen Wang[1] ✉

Unraveling how reactive facets promote photocatalysis at the molecular level remains a grand challenge, while identification of the reactive facets can provide guidelines for designing highly efficient photocatalysts and unravelling the microscopic mechanisms behind them. Recently, a series of polytriazine imides (PTIs) was reported with highly crystalline structures; all had a relatively low photocatalytic activity for overall water splitting. Here, high-angle annular dark-field scanning transmission electron microscopy, energy dispersive spectroscopy mapping, and aberration-corrected integrated differential phase contrast imaging were used to study PTI/Li$^+$Cl$^-$ single crystals before and after in situ photodeposition of co-catalysts, showing that the prismatic $\{10\bar{1}0\}$ planes are more photocatalytically reactive than the basal {0001} planes. Theoretical calculations confirmed that the electrons are energetically favourable to transfer toward the $\{10\bar{1}0\}$ planes. Upon this discovery, PTI/Li$^+$Cl$^-$ crystals with different aspect ratios were prepared, and the overall water splitting performance followed a linear correlation with the relative surface areas of the $\{10\bar{1}0\}$ and {0001} planes. Our controlling of the reactive facets directly instructs the development of highly efficient polymer photocatalysts for overall water splitting.

Photocatalytic water splitting using semiconductors and sunlight promises the production of clean and renewable hydrogen gas to supply energy and feedstock for hydrocarbon and alcohol production[1–4]. However, some key issues need to be solved to enable the practical application of this environmentally benign technology[5–9]. It is well known that the reactive facets of heterogeneous photocatalysts play an important role during the water photolysis process because they afford the active sites/planes for the photoredox splitting of water or loading of co-catalysts[10]. Therefore, photocatalytic performance largely depends on the exposed reactive facets. For example, the {001} facets of inorganic photocatalyst TiO_2 were found to be more reactive than the commonly exposed {101} facets. Increasing the exposed surface areas of {001} facets leads to substantially enhanced photocatalytic activity of TiO_2 (refs. [11–13]). Such structure–property correlation also holds for other inorganic photocatalysts, such as Ag_3PO_4, WO_3 and $SrTiO_3$ (refs. [14–16]). Recent studies indicated that the facets also play additional roles during the photocatalytic process, namely, charge separation. Taking $BiVO_4$ as an example, it was found that the photo-reduction reaction occurred on {010} facets, while the photo-oxidation reaction proceeded on {110} facets, indicating that the photogenerated electrons and holes can be efficiently separated on different crystal facets[17]. Therefore, identification of reactive facets and exploring how the reactive facets facilitate the reactivity is considered to be a crucial step for the development of high-performance photocatalysts for solar to chemical conversion.

Investigations of the reactive facets have mainly focused on inorganic photocatalysts. Recently, polymeric carbon nitride (PCN) has attracted great interest in photocatalytic water splitting due to its unique properties[18–22]. Prior studies suggested that the two-dimensional (2D) planes of PCN were reactive facets due to the highly exposed surface areas as well as the suitable coordination environment for the incorporation of co-catalysts[23–26]. However, studies regarding the exact reactive facets of this conjugated polymer have rarely been reported for two major reasons: First, PCN prepared by traditional thermally induced polymerization typically exhibits low crystallinity. Second, those polymers are not stable under the irradiation of high-energy electron beams[27]. Those two factors together largely hinder the understanding of PCN's exact atomic structure and the identification of the role of its reactive planes in the promotion of water photolysis.

Many synthetic strategies have been developed to prepare crystalline PCN[28–31]. Among them, PTI intercalated with LiCl (PTI/Li$^+$Cl$^-$) synthesized by ionothermal methods has been demonstrated to be highly crystalline and can achieve photocatalytic overall water splitting by the loading of suitable co-catalysts[32,33]. In this regard, PTI/Li$^+$Cl$^-$ forms an ideal system for the exploration of the reactive facets of conjugated polymers.

In this report, a transmission electron microscopy (TEM) technique, aberration-corrected integrated differential phase contrast (AC-iDPC) imaging, was adopted to study the atomic structure, especially the surface structures of PTI/Li$^+$Cl$^-$ under an extremely low electron dose rate. Moreover, photodeposition of Co and Pt co-catalysts was used to probe the reactive facets of PTI/Li$^+$Cl$^-$ in overall water photolysis. Strikingly, all those experiments demonstrated that the side prismatic planes $\{10\bar{1}0\}$ were the major reactive facets, different from conventional wisdom on PCN nanosheets. First principles calculations were also performed to understand the electronic structures and confirm the electron–hole transition among the prismatic $\{10\bar{1}0\}$ planes of the PTI/Li$^+$Cl$^-$. Hence, crystal engineering by enlarging the side planes, that is, increasing the thickness of the conjugated layers, provides an alternative pathway to improve the photoactivity of layered conjugated polymers. We found that the photocatalytic activity followed an approximately linear correlation with the surface area ratio of $\{10\bar{1}0\}$ and {0001} of the PTI/Li$^+$Cl$^-$ crystals, confirming the feasibility of our proposed

---

[1]State Key Laboratory of Photocatalysis on Energy and Environment, College of Chemistry, Fuzhou University, Fuzhou, P. R. China. [2]College of Chemical Engineering, Fuzhou University, Fuzhou, P. R. China. ✉e-mail: xcwang@fzu.edu.cn

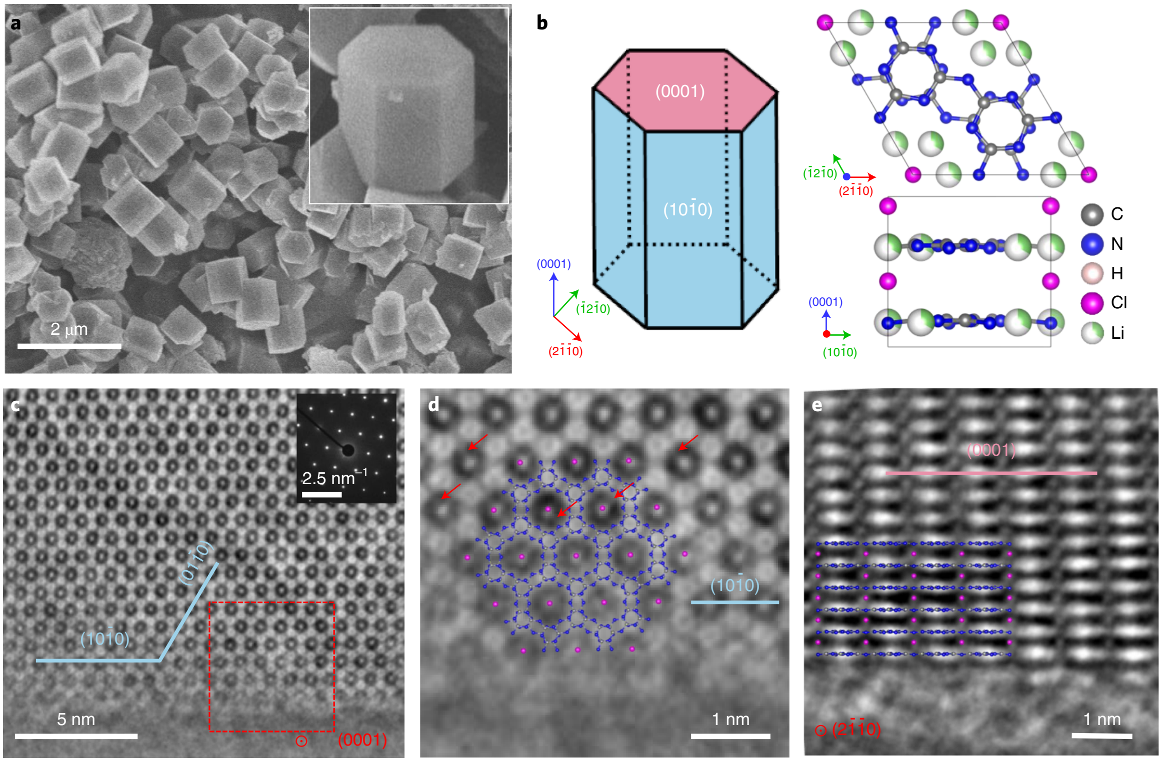

Fig. 1 | The morphology and atomic structure of PTI/Li$^+$Cl$^-$. a, SEM image showing the well-developed prism-like shape of PTI/Li$^+$Cl$^-$ crystals. The inset shows the expanded view of a crystal. **b**, Left, schematic illustration of the PTI/Li$^+$Cl$^-$ crystal with the basal plane terminated by two {0001} planes and the side faces terminated by six equivalent {10$\bar{1}$0} facets. Right, the crystal structure of PTI/Li$^+$Cl$^-$ (Li is at 1/3 occupation). **c**, The AC-iDPC images of a typical PTI/Li$^+$Cl$^-$ crystal aligned along the [0001] direction. The inset shows the corresponding diffraction pattern. **d**, Expanded view of the red box in **c**. The positions of C, N and Cl atoms are superimposed. Some typical Li ions are denoted by red arrows. **e**, The AC-iDPC images of a typical PTI/Li$^+$Cl$^-$ crystal aligned along the [2$\bar{1}\bar{1}$0] direction.

strategy and facilitating the optimization of polymeric photocatalysts for solar fuel production.

Results

Synthesis of PTI/Li$^+$Cl$^-$ samples. The PTI/Li$^+$Cl$^-$ samples were prepared by an ionothermal method[32]. First, dicyandiamide (DCDA) was mixed with KCl/LiCl and preheated in air in a glass tube to release ammonia gas. Then, the glass tube was evacuated to a high vacuum and sealed by a flamer. Finally, the sealed tube was heated at a certain temperature to prompt the crystallization of the conjugated polymer. After cooling, the sample was collected by filtration followed with drying in a vacuum.

Determination of the reactive surfaces. The as-prepared product is predominantly composed of crystals with sizes of several hundred nanometres, as shown in the scanning electron microscopy (SEM) image (Fig. 1a). The prominent prism profile (inset of Fig. 1a) is distinctly different from the conventional bulk PCN produced by direct thermal polymerization of N-containing precursors[34]. This difference indicates the high crystallinity, confirming a complete crystallization of PTI/Li$^+$Cl$^-$. All the crystals were enclosed by two hexagonal {0001} facets as basal planes and six rectangular {10$\bar{1}$0} facets as prismatic planes (or side planes), as schematically illustrated in Fig. 1b. Here, we employed the AC-iDPC technique that integrates the merits of low-dose imaging and imaging of heavy and light atoms with high contrast to investigate their atomic structures. The iDPC image is a very good approximation of an ideal centre of mass[35]. It produces two images proportional to the gradients of the phase of the sample, the integration of which is directly proportional to the phase itself[36]. Hence, the bright spots in iDPC images correspond to atoms, allowing simple image interpretation.

As shown in Fig. 1c, an AC-iDPC image of a typical crystal projected along a [0001] zone axis reveals the periodic contrasts without any observable defects, indicating the high atomic ordering of the PTI/Li$^+$Cl$^-$. The high crystallinity is confirmed by the corresponding fast fourier transform (FFT) in the inset of Fig. 1c. Figure 1d,e presents the high-resolution iDPC image of the PTI crystals aligned along the two orthogonal [0001] and [2$\bar{1}\bar{1}$0] directions, respectively. Several important findings emerge after careful image analysis. First, the intensity of each column directly reflects the projected atomic potential and bright spots correspond to atomic columns. The constitutional atoms, such as C, N and Cl, are clearly resolved, without the necessity of tedious image simulation. Confirmed by our high resolution electron microscopy (HREM) and iDPC image simulations (Supplementary Figs. 1–3), the bright spots in iDPC images simply correspond to atomic columns, contrasting somewhat with the complicated situation in HREM images. Even some Li cations randomly distributed on the 6c site (Space group: P6$_3$mc) could be resolved, albeit with relatively low contrast. Six-membered C$_3$N$_3$ rings form honeycomb-like skeletons and Cl anions fill in the interstices (see Fig. 1b,d). Second, the six prismatic planes of the PTI/Li$^+$Cl$^-$ crystal are set to edge-on conditions along the *c* axis (Fig. 1d) and the side faces are invariably terminated by Cl cations. Third, different from the {10$\bar{1}$0} side faces, the {0001} basal planes expose carbon and nitrogen atoms in the exterior surface. Last, dense {0001} conjugated layers are found to be separated by Cl anions (Fig. 1b,e). As a result, the atomic structure of PTI crystals is proposed on the basis of the AC-iDPC images projected

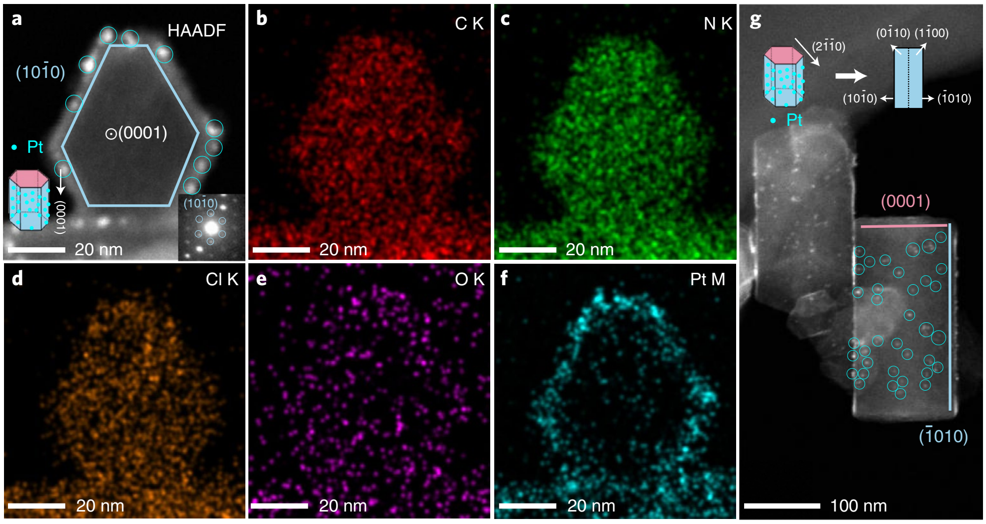

Fig. 2 | The spatial distribution of the Pt co-catalysts after photodeposition. a, The HAADF-STEM image of a PTI crystal aligned close to the [0001] direction; the inset shows the diffraction pattern from the particle. Note that the side faces correspond to the {10$\bar{1}$0} facets. **b–f**, EDS maps of the main constitutional elements. **g**, The HAADF-STEM image of a PTI crystal aligned to the [2$\bar{1}\bar{1}$0] direction. The inset shows a schematic illustration of the distribution of Pt particles on the surfaces of PTI crystals. The blue circles indicate the positions of Pt particles (**a**,**g**).

along two orthogonal directions, which is in line with previous literature[29,37]. Moreover, our iDPC images, simulated on the basis of reconstructed structures, match well with our experimental ones (Supplementary Figs. 1–3). Unfortunately, it is difficult to determine the sites of H by AC-iDPC due to its small atomic number; hydrogen and lithium elements were detected by elemental analysis and inductively coupled plasma analysis (Supplementary Table 1). The plausible position of H atoms was adapted (Fig. 1b) from previous literature[29], where H exists in the form of an amino group. More details on the surface structure of {10$\bar{1}$0} planes are presented in Supplementary Fig. 4.

As demonstrated in previous works, Pt and Co clusters can be photodeposited on the surfaces of PTI/Li$^+$Cl$^-$ as the reduction and oxidation co-catalysts for photocatalytic overall water splitting[33,38]. Those co-catalysts can be used as probes to track the reactive facets. Thus, we combined high-angle annular dark-field scanning transmission electron microscopy (HAADF-STEM) and energy dispersive spectroscopy (EDS) mapping to investigate the distribution of the co-catalysts after photocatalytic deposition. Figure 2a displays the HAADF-STEM image after photodeposition. Figure 2b–e shows that the C, N, Cl and O elements are distributed uniformly within the samples. Pt clusters prefer to sit on the border of hexagons (see the lines in Fig. 2a as a guide) that are the projection of PTI crystals along the [0001] axis. Bright spots were found on the prismatic {10$\bar{1}$0} planes rather than the {0001} planes. To elucidate the deposited sites of Pt particles, we further examined them along the [$\bar{1}$2$\bar{1}$0] direction that is perpendicular to the [0001] direction (Fig. 2g). We found that Pt particles were photodeposited homogenously on {10$\bar{1}$0} planes, while {0001} planes had negligible Pt particles. Moreover, PTI crystals were enclosed by flat facets, rather than stacked carbon nitride sheets with surface edges (Supplementary Fig. 5).

Similar results were also found with the Co co-catalyst, as shown in Supplementary Fig. 6, where the Co co-catalysts tend to deposit, again, on the {10$\bar{1}$0} planes. The photogenerated electron–hole pairs were confined on the π-conjugated {0001} plane. Coincidently, the {10$\bar{1}$0} facets, as the destination of the charge carriers, were terminated by Cl anions. As a result, the co-catalysts were anchored on the {10$\bar{1}$0} facets where the electrons or holes were driven. The situation was different for the {0001} facets[39], because most of the electrons and holes had difficulty crossing the conjugated layers. Therefore, both Pt and Co co-catalysts favour being photodeposited on the {10$\bar{1}$0} planes. To gain deep insight into the transfer of the photogenerated electron–hole pairs along the conjugated layers, temperature-dependent photoluminescence (TD-PL) was performed to extract the exciton binding energy (EBE) of PTI/Li$^+$Cl$^-$ (Supplementary Fig. 7)[40,41]. The EBE of PTI/Li$^+$Cl$^-$ was determined to be 50.4 meV. Although this value is much lower than that of some conjugated polymers[42,43], the EBE of PTI/Li$^+$Cl$^-$ is still greater than the thermal disturbance energy (~26 meV at room temperature), suggesting that the transfer of photogenerated electron–hole pairs would be favourable as excitons rather than as free electrons and holes, in agreement with the results obtained from organic photovoltaic cells[44,45]. Overall, both the reduction and oxidation reactions induced by photoexcitation tended to occur in the same crystal planes, which is different from the $BiVO_4$ photocatalyst where the photo-reduction and photo-oxidation co-catalysts are selectively deposited on the {010} and {110} facets, respectively[17].

To understand the electron structure properties of the PTI/Li$^+$Cl$^-$ crystals, density functional theory (DFT) calculations were carried out on the basis of the proposed crystal structure. The structure is given in Fig. 3a, and the corresponding charge density maps on a (0001) and (10$\bar{1}$0) plane are presented in Fig. 3b,c, respectively. As shown in Fig. 3b, the charge density concentrated on the conjugated layers, that is, the (0001) plane, while the charge density between the layers (Fig. 3c) is much less dense. The analysis of the electron structure assumes that the photogenerated carriers prefer in-plane migration other than interlayer hopping. This claim is supported by the fact that the potential well of interlayer electron hopping is much higher than potential wells of in-plane electron hopping (Supplementary Fig. 8). Hence, the {10$\bar{1}$0} planes are suspected to be the major reactive planes, if the photogenerated carriers of the bulk and surface can be captured on the active sites.

To unravel in detail how the photogenerated carriers transfer on PTI/Li$^+$Cl$^-$ with the Pt co-catalyst, the transition dipole moments between the valence bands (VBs) and the conduction bands (CBs) of a Pt_8 cluster adsorbed on the (10$\bar{1}$0) plane of PTI/Li$^+$Cl$^-$ were calculated. A subnanometre Pt_8 cluster was used to mimic the several-nanometre size of the experimental Pt co-catalyst on PTI, due to the computational demand and a recent general guideline for studying the photoelectron transfer of the size effect of Pt co-catalyst on a TiO_2 support[46,47]. Adsorption of the Pt_8 cluster generates a series of bands (red lines in Fig. 3d) among those contributed

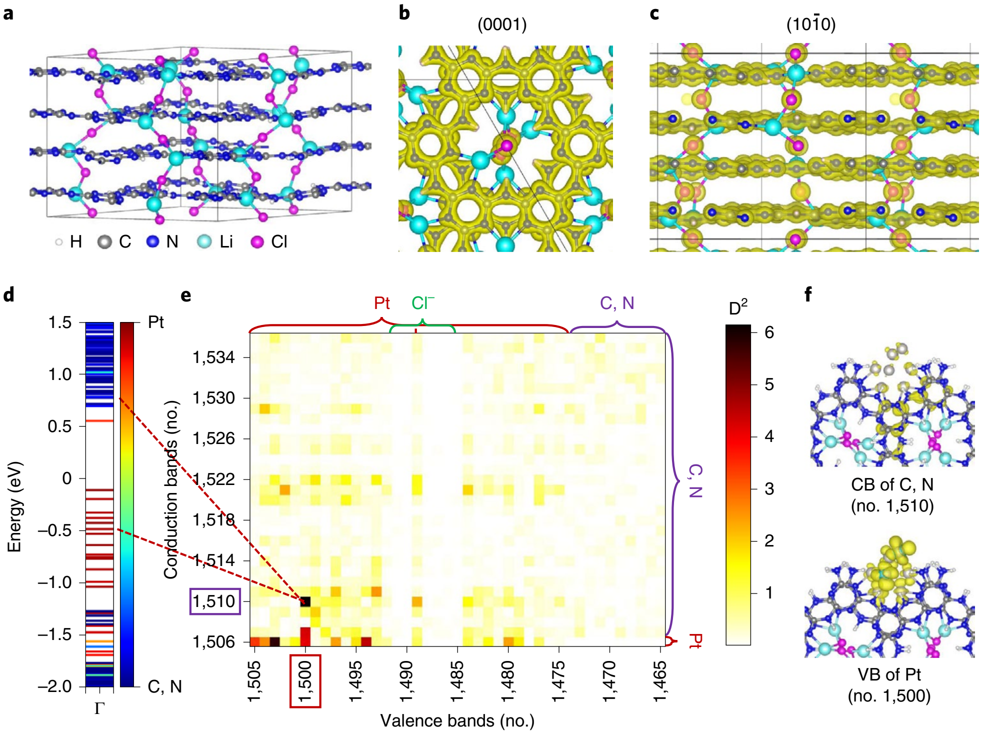

Fig. 3 | The electronic structure properties. **a**, The computational PTI/Li$^+$Cl$^-$ model. **b**,**c**, Charge density of PTI/Li$^+$Cl$^-$ along the (0001) and (10$\bar{1}$0) crystal planes, respectively. **d**, Projected band structure (Γ-point, spin up) of Pt$_8$ adsorbed on the (10$\bar{1}$0) crystal plane of PTI/Li$^+$Cl$^-$. **e**, Transition dipole moments between VBs and CBs. The red dashed lines pointing to lines in **d** indicate the corresponding VB (no. 1,500) and CB (no. 1,510). **f**, Charge density of Pt$_8$@PTI/Li$^+$Cl$^-$ with band numbers of 1,510 (CB of C, N) and 1,500 (VB of Pt).

from the PTI/Li$^+$Cl$^-$. As shown in Fig. 3e, although the bands of Cl$^-$ sit among the VB region (bands around 1,490), the transition probability between CBs and Cl$^-$ bands is negligible, proving that the destination of the charge carriers is terminated by Cl$^-$ anions. On the other hand, high transition probabilities occur between the CBs contributed from C and N (bands with no. 1,507 and up) and the VBs attributed to Pt (bands with nos 1,505 to 1,475). The highest transition probability happens between the VB of Pt (band no. 1,500) and the CB of C and N (band no. 1,510), as shown in Fig. 3f. Hence, the computed results show that the {10$\bar{1}$0} planes with the photodeposited Pt clusters are preferred as the major reactive sites, as the photogenerated carriers from the bulk and surface can be captured on them.

The {10$\bar{1}$0} facets were determined to be the primary reactive facets of PTI/Li$^+$Cl$^-$. Therefore, a promising strategy to enhance its photocatalytic activity is to enlarge the prismatic surfaces by increasing the surface areas of the {10$\bar{1}$0} facets; that is, crystals with a rod shape would possess better photocatalytic activity.

Tuning the surface area ratio of {10$\bar{1}$0} and {0001} planes. Some methods can be used to control the growth of a specific crystal plane, such as using surfactant in solvothermal synthesis[48]. However, the ionothermal temperatures are typically above 450 °C, which would destroy most organic solvents. Previous work has demonstrated that the length of PTI/Li$^+$Cl$^-$ prisms can be adjusted using a synthetic temperature[32]. Therefore, we focus on the dependence of the photocatalytic activity on synthetic temperature in this work. Three typically synthetic temperatures, 500, 550 and 600 °C, were applied, and the corresponding samples were named PTI-500, PTI-550 and PTI-600, respectively.

The as-obtained samples were characterized by multiple techniques to acquire their intrinsic properties. Powder X-ray diffraction patterns with sharp peaks were observed in all PTI/Li$^+$Cl$^-$ samples, indicating the good crystallinity (Supplementary Fig. 9a). All the samples were determined to be hexagonal phases with $P6_3mc$ symmetry (space group 185) with similar lattice parameters (Supplementary Table 2). Fourier transform infrared (FTIR) spectra of samples (Supplementary Fig. 9b) exhibit stretching vibration bands of the amino groups at 3,300–3,200 cm^{-1} and C–N stretching and bending vibrations of the triazine rings at 1,700–1,100 cm^{-1}, together with a vibrational fingerprint of triazine heterocycles at 808 cm^{-1}. Similar vibration properties were also observed in Raman spectra (Supplementary Fig. 9c). As shown in Supplementary Fig. 9d, typically semiconductor-like absorptions were found for those samples. Notably, the absorption edge and intensity of the three batches of samples are similar. The bandgap of those samples, estimated from the absorption edge, was 3.1 eV, which is larger than that of the typical heptazine-based PCN (2.7 eV)[18]. This is because PTI is composed of triazine subunits connected by imide, leading to the reduced π-conjugated system. Furthermore, the surface areas are 33, 36 and 42 m^2 g^{-1} for the PTI-500, PTI-550 and PTI-600, respectively (Supplementary Fig. 10). Last, the elemental contents of the three samples were nearly identical, as presented in Supplementary Table 1. Overall, the intrinsic properties of the samples exhibit stability at synthetic temperatures ranging from 500 to 600 °C.

SEM analysis was carried out to further investigate the influence of synthetic temperature on the morphologies of the samples. As shown in the inset of Fig. 4a, PTI-500 exhibited a plate-like microstructure. In PTI-550 the crystals were rod-like. Increasing the synthetic temperature to 600 °C led to a reduction in particle sizes. The morphologies found by TEM analysis were consistent with the SEM results (Supplementary Fig. 11). We conducted quantitative analysis of the surface area (S) ratio of the {10$\bar{1}$0} and {0001} planes of the samples (Supplementary Fig. 12). The average $S_{\{10\bar{1}0\}}/S_{\{0001\}}$

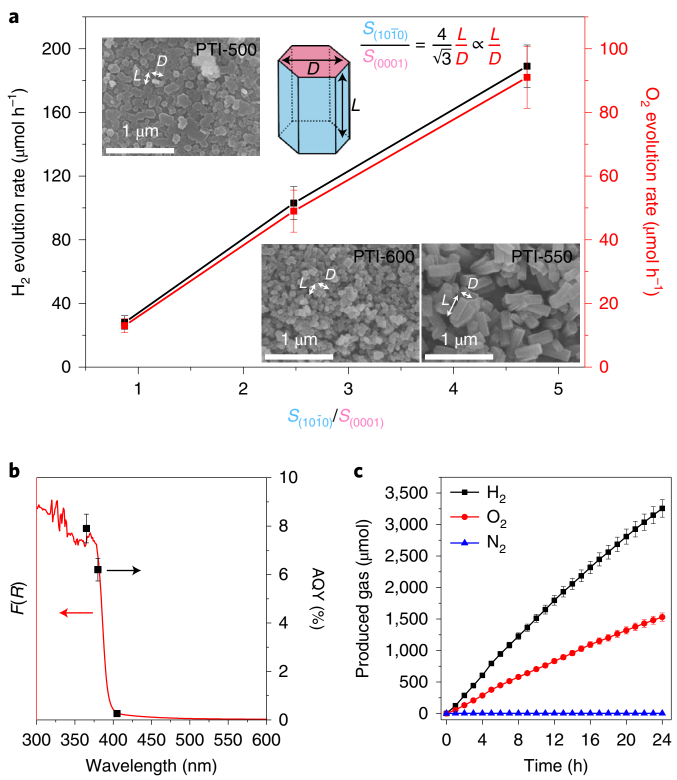

Fig. 4 | Photocatalytic performances. a, The plot of maximum hydrogen and oxygen evolution rate as a function of the mean surface area ratio of the $\{10\bar{1}0\}$ and $\{0001\}$ planes $\left(S_{\{10\bar{1}0\}}/S_{\{0001\}}\right)$ of the samples. The insets show three typical SEM images of PTI crystals synthesized at different temperatures. The coloured diagram and equation indicate that $S_{\{10\bar{1}0\}}/S_{\{0001\}}$ is proportional to the aspect ratio. **b**, Wavelength-dependent AQY of PTI-550. *F*(*R*), the Kubelka–Munk function with the reflectivity (*R*). **c**, The accumulated amount of the gases produced by PTI-550 (evacuated at each hour after sampling). The error bars show standard deviation.

values obtained from statistical sampling are 0.87, 4.70 and 2.48 for PTI-500, PTI-550 and PTI-600, respectively (Fig. 4a).

Photocatalytic overall water splitting. Water photolysis was carried out to check the performance of the as-obtained samples with different aspect ratios. Pt/Co co-catalysts were loaded on all samples by the photodeposition method. The photocatalytic overall water splitting performance was found to follow an approximately linear correlation with the surface area ratio of the $\{10\bar{1}0\}$ and $\{0001\}$ planes, further confirming that the photoactivities of the PTI/Li$^+$Cl$^-$ crystals strongly depend on the exposed surfaces of the reactive facets (Fig. 4a). Incidentally, $S_{\{10\bar{1}0\}}/S_{\{0001\}}$ is proportional to the aspect ratios, as we derived in the inset of Fig. 4a. The maximum hydrogen and oxygen evolution rates of the PTI-550 reached 189 and 91 μmol h^{-1}, respectively, at a $S_{\{10\bar{1}0\}}/S_{\{0001\}}$ ratio of 4.70, much higher than in a prior study[33]. By contrast, the PTI-500 and PTI-600 samples, with lower $S_{\{10\bar{1}0\}}/S_{\{0001\}}$ ratios, exhibit a much lower photoactivity than that of PTI-550. The wavelength-dependent apparent quantum yield (AQY) of the PTI-550 is depicted in Fig. 4b, in which the AQY value matches well with the diffuse reflectance spectra (DRS) pattern, indicating that the overall water splitting is induced by the absorption of the incident light.

Several additional experiments were carried out to check the photocatalytic performance of PTI-550. First, very little gas was produced by PTI without co-catalysts (Supplementary Fig. 13). This result indicates that electrons and holes are separated by Pt and Co co-catalysts. Second, deactivation was observed in the second hour (Supplementary Fig. 14). X-ray diffraction and FTIR patterns of PTI-550 before and after photoreaction are similar to each other, indicating that the crystallinity and chemical structure are maintained (Supplementary Fig. 15). Therefore, the deactivation might relate to back-reaction on the surface of the photocatalyst. To prove our hypothesis, a controlled experiment was carried out by evacuating the gas produced at each hour after sampling. As shown in Fig. 4c and Supplementary Fig. 16, the stability was substantially improved and the molar ratio of H$_2$ and O$_2$ gases is close to two at each hour, suggesting that the deactivation is primarily ascribed to the back-reaction. Third, the gases produced were stabilized by periodic evacuation even when the photoreaction duration was extended to 96 h. No substantial change of crystal structures was observed (Supplementary Fig. 17), further implying the high stability of the $\{10\bar{1}0\}$ reactive surfaces. Decreased performance in the beginning 48 h was observed, presumably due to the agglomeration or detachment of the co-catalysts. These issues may be solved by elaborately designing the nanoarchitecture of the co-catalyst to prevent the reverse reaction and enhance its stability[49]. Fourth, the water splitting performance decreased by about 20% if we deposited Pt particles before Co. Fifth, the activity increased ~15% after grinding for an extra 30 min (Supplementary Fig. 18). Last, overall water splitting was carried out at 1 bar of Ar gas. The activity decreased to about one-sixth compared with that at reduced pressure (Supplementary Fig. 19) due to the difficulty in the detachment of the bubbles. Nevertheless, the H$_2$ and O$_2$ produced can still be observed, which holds great promise for practical application under ambient pressure.

Conclusion

In summary, we have identified the reactive facets of PTI/Li$^+$Cl$^-$ by using Pt/Co as co-catalysts for photocatalytic overall water splitting. Our results confirm that the prismatic surfaces are the primary reactive facets because of two factors: the photogenerated electron–hole pairs can easily migrate along the conjugated layers to the $\{10\bar{1}0\}$ facets, and the co-catalysts are mostly photodeposited on the $\{10\bar{1}0\}$ facets due to the more-available electrons or holes on the prismatic surfaces. The reactive facets were tuned by changing the surface area ratios. The results showed that increasing the prismatic surface areas (reactive facets) can greatly enhance the performance of PTI/Li$^+$Cl$^-$ in the photocatalytic overall water splitting reaction. The photocatalytic overall water splitting performance on PTI-550 showed an AQY of 8% at 365 nm. In contrast with the preparation of PCN nanosheets, this work provides a design strategy to boost the photoactivity of layered conjugated polymers in a one-step-excitation overall water splitting reaction.

Methods

Preparation of PTI/Li$^+$Cl$^-$ samples. DCDA (1 g) was ground with potassium chloride (5.5 g) and lithium chloride (4.6 g) in a glove box under a high-purity nitrogen atmosphere. The mixed precursor was loaded into a glass tube (Φ_{out} = 3.2 cm and Φ_{in} = 2.8 cm, where Φ refers to the diameter, length = 18 cm) and heated to 400 °C for 4 h with a ramp rate of 2 °C min^{-1} in a muffle furnace. After naturally cooling, the tube was evacuated and sealed. The sealed tube was heated to a certain temperature (*T*) for 24 h with a ramp rate of 1 °C min^{-1} in a muffle furnace. After cooling to room temperature naturally, the tube was carefully opened and the sample was taken out by ultrasonication in deionized water. The sample was further washed with boiling deionized water and filtered to remove residual salt. The conductivity of the filtrate was measured to determine the end point of washing. Finally, the samples were dried in the vacuum oven at 60 °C. The resulting samples were collected and ground into powders with an agate mortar for further use. The samples were denoted PTI-*T* (*T* = 500, 550 and 600) using the different final calcination temperatures. The synthetic procedure of the PTI crystal for AC-iDPC imaging and reactive facet analysis was similar to that of PTI-550 but with a ramp rate of 6 °C min^{-1} and holding time of 12 h.

Characterization and image simulation. Powder X-ray diffraction measurements were performed on a Bruker D8 Advance diffractometer with Cu-Kα1 radiation (λ = 1.5406 Å). SEM was performed on a HITACHI SU-8010 field emission scanning electron microscope. TEM and EDS mapping were performed on a Thermo Fisher Scientific microscope (Talos F200S). Spherical aberration corrected TEM (AC-TEM) examination, including iDPC imaging, was carried out on Thermo Fisher Scientific Themis Z located in the Netherlands. For good iDPC imaging, we searched the thinnest crystals, with a sample thickness around 20 nm. The aberration coefficient was as follows: A1 = 2.1 nm, A2 = 15.5 nm, B2 = 45.1 nm, C3 = 306 nm, A3 = 169 nm, S3 = 329 nm, A4 = 3.47 µm, D4 = 12.7 µm and B4 = 4.4 µm. The dose rate for our high-resolution iDPC images was about 1,000 $e\,s^{-1}$ Å^{-2}.

The principle of iDPC imaging is shown in Supplementary Fig. 20. The iDPC technique integrates the merits of easy, low-dose imaging; imaging heavy and light atoms with high contrast; and intuitive image interpretation (see Supplementary Figs. 1–3 for our simulated iDPC image of PTI crystals) in that bright spots directly correspond to atomic potentials[36]. The technique is now being widely adopted by the chemistry community to characterize soft materials composed of light and heavy elements at a decent thickness[50].

STEM-iDPC images were simulated using a self-developed multi-slice image simulation code based on Kirkland's original code[51]. First, we simulated four-sector ADF images using a collection angle of 8–30 mrad. The aberration coefficients were adopted from the experiment. We simulated images at varied thickness and defocus values. Then, those four-sector ADF images were processed following a published procedure[36]. Similarly, HREM images were also simulated with our codes, for comparison.

To obtain interpretable EDS maps, the EDS mapping parameters were optimized, because PTI is sensitive to the electron beam. We utilized a probe with a 200 pA current. EDS mapping proceeded at lower magnifications over a scanning area of 100 nm × 100 nm to reduce the dose rate. The dwell time of each pixel was 1 µs to avoid a discernable morphology change of the PTI particles. Scanning was stopped at about 200 s when the Pt maps exhibited a decent signal. The measured dose rate was $2.5\times10^{5}\,e\,s^{-1}$ Å^{-2}. No discernable Pt sputtering or morphology damage of the PTI crystals (Supplementary Fig. 21) was found. The positions of Pt particles were intact during EDS mapping.

The ultraviolet–visible DRS (UV-Vis DRS) were measured on a Varian Cary 500 Scan UV-Vis system. FTIR spectra were recorded on a Nicolet iS50 spectrometer. Elemental analysis was carried out on an Elementar Vario EL Cube. Inductively coupled plasma emission spectrometry was conducted on a PerkinElmer Avio 200. Nitrogen adsorption–desorption isotherms were measured at 77 K using Micromeritics ASAP 2460 equipment. The PL spectra were recorded on a HORIBA Fluorolog-3 spectrophotometer. The EBE was estimated according to the following equation:

$$I(T) = \frac{I_0}{1 + \mathrm{e}^{-\frac{E_\mathrm{b}\ T}{k_\mathrm{B}}}} \tag{1}$$

where the I_0 is the intensity at 0 K, k_B is the Boltzmann constant and E_b is the EBE.

Details of the calculations. All spin-polarized DFT calculations were done through the Vienna ab initio simulation package (VASP) version 5.4 (refs. [52,53]). Projector augmented wave (PAW) potentials[54,55] were used to describe the electron–ion interactions, and the generalized gradient approximation (GGA) of the Perdew, Burke and Ernzerhof (PBE) functional was used to describe the exchange and correlation interactions[56]. The van der Waals corrections were considered via Grimme's D2 method[57]. The wave function was expanded using plane waves with a cut-off energy of 520 eV. The Brillouin zone was sampled with a Γ-point[58]. The systems were fully relaxed until the conventional energy was smaller than 10^{-6} eV and the Hellmann–Feynman forces were smaller than 0.02 eV Å^{-1}. The PTI/Li$^+$Cl$^-$ and Pt$_8$@PTI/Li$^+$Cl$^-$ were modelled using a $\sqrt{3}\times\sqrt{3}\times4$ supercell.

Loading of Pt/Co co-catalyst. The set-up and procedure of the photodeposition were similar to that of the photocatalytic overall water splitting test. The photocatalyst (120 mg) was first photodeposited of 0.5 wt% Co co-catalyst in 100 ml deionized water using $CoCl_2{\cdot}6H_2O$ under full-spectrum irradiation of a 300 W xenon lamp. After 2 h photoreaction, the reactor was opened and $H_2PtCl_6{\cdot}6H_2O$ solution (1.0 wt% Pt) was dropped into the reaction solution. The reactor was evacuated again and irradiated with full-spectrum irradiation of the xenon lamp for another 2 h. Then the Pt/Co-loaded photocatalyst was collected by filtration and washed with deionized water several times. The resulting photocatalyst powder was dried at 60 °C overnight.

Photocatalytic overall water splitting. Reactions were carried out in a Pyrex top-irradiation reaction vessel connected to a closed glass gas system. The Pt/Co-loaded photocatalyst (100 mg) was dispersed into 100 ml deionized water. The reaction solution was evacuated several times to remove air completely prior to irradiation under a 300 W xenon lamp (>300 nm). The temperature of the reaction solution was maintained at room temperature by the flow of cooling water during the reaction. The evolved gases were analysed by gas chromatography (Shimadzu, GC-8A), with a thermal conductive detector and 5 Å molecular sieve column, using Ar as the carrier gas.

The AQY of the overall water splitting was measured with a similar set-up. The difference was that we replaced the xenon lamp with monochromatic-light light-emitting diodes (LEDs) equipped with corresponding bandpass filters. The irradiation area was controlled to be 9 cm^2. The total intensity of irradiation was measured by an optical power meter (Newport 2936-R). For example, the intensity was 6.6 mW cm^{-2} for 380 nm monochromatic light. The AQY was calculated using the following equation:

$$\mathrm{AQY}\ (\%) = \frac{(\mathrm{Number\ of\ evolved\ H_2\ molecules} \times 2)}{(\mathrm{Number\ of\ incident\ photons})} \times 100\% \tag{2}$$

Data availability

The data that support the findings of this study are available from the corresponding author upon reasonable request.

Received: 13 November 2019; Accepted: 26 May 2020;
Published online: 29 June 2020

References

1. Fujishima, A. & Honda, K. Electrochemical photolysis of water at a semiconductor electrode. *Nature* **238**, 37–38 (1972).
2. Lewis, N. S. Research opportunities to advance solar energy utilization. *Science* **351**, aad1920 (2016).
3. Chen, S., Takata, T. & Domen, K. Particulate photocatalysts for overall water splitting. *Nat. Rev. Mater.* **2**, 17050 (2017).
4. Chen, X., Shen, S., Guo, L. & Mao, S. S. Semiconductor-based photocatalytic hydrogen generation. *Chem. Rev.* **110**, 6503–6570 (2010).
5. Maeda, K. et al. Photocatalyst releasing hydrogen from water. *Nature* **440**, 295–295 (2006).
6. Yu, J. & Kudo, A. Effects of structural variation on the photocatalytic performance of hydrothermally synthesized $BiVO_4$. *Adv. Funct. Mater.* **16**, 2163–2169 (2006).
7. Zong, X. et al. Enhancement of photocatalytic H_2 evolution on CdS by loading MoS_2 as cocatalyst under visible light irradiation. *J. Am. Chem. Soc.* **130**, 7176–7177 (2008).
8. Wang, Q. et al. Scalable water splitting on particulate photocatalyst sheets with a solar-to-hydrogen energy conversion efficiency exceeding 1%. *Nat. Mater.* **15**, 611–615 (2016).
9. Wang, Z. et al. Overall water splitting by Ta_3N_5 nanorod single crystals grown on the edges of $KTaO_3$ particles. *Nat. Catal.* **1**, 756–763 (2018).
10. Liu, G., Yu, J. C., Lu, G. Q. & Cheng, H.-M. Crystal facet engineering of semiconductor photocatalysts: motivations, advances and unique properties. *Chem. Commun.* **47**, 6763–6783 (2011).
11. Yang, H. G. et al. Anatase TiO_2 single crystals with a large percentage of reactive facets. *Nature* **453**, 638–641 (2008).
12. Yu, J., Qi, L. & Jaroniec, M. Hydrogen production by photocatalytic water splitting over Pt/TiO_2 nanosheets with exposed (001) facets. *J. Phys. Chem. C* **114**, 13118–13125 (2010).
13. Han, X. et al. Synthesis of titania nanosheets with a high percentage of exposed (001) facets and related photocatalytic properties. *J. Am. Chem. Soc.* **131**, 3152–3153 (2009).
14. Bi, Y. et al. Facet effect of single-crystalline Ag_3PO_4 sub-microcrystals on photocatalytic properties. *J. Am. Chem. Soc.* **133**, 6490–6492 (2011).
15. Zhang, J., Zhang, P., Wang, T. & Gong, J. Monoclinic WO_3 nanomultilayers with preferentially exposed (002) facets for photoelectrochemical water splitting. *Nano Energy* **11**, 189–195 (2015).
16. Mu, L. et al. Enhancing charge separation on high symmetry $SrTiO_3$ exposed with anisotropic facets for photocatalytic water splitting. *Energy Environ. Sci.* **9**, 2463–2469 (2016).
17. Li, R. et al. Spatial separation of photogenerated electrons and holes among {010} and {110} crystal facets of $BiVO_4$. *Nat. Commun.* **4**, 1432 (2013).
18. Wang, X. et al. A metal-free polymeric photocatalyst for hydrogen production from water under visible light. *Nat. Mater.* **8**, 76–80 (2009).
19. Zheng, Y., Lin, L., Wang, B. & Wang, X. Graphitic carbon nitride polymers toward sustainable photoredox catalysis. *Angew. Chem. Int. Ed.* **54**, 12868–12884 (2015).
20. Ong, W.-J. et al. Graphitic carbon nitride (g-C_3N_4)-based photocatalysts for artificial photosynthesis and environmental remediation: are we a step closer to achieving sustainability? *Chem. Rev.* **116**, 7159–7329 (2016).
21. Cao, S., Low, J., Yu, J. & Jaroniec, M. Polymeric photocatalysts based on graphitic carbon nitride. *Adv. Mater.* **27**, 2150–2176 (2015).
22. Kessler, F. K. et al. Functional carbon nitride materials—design strategies for electrochemical devices. *Nat. Rev. Mater.* **2**, 17030 (2017).
23. Wang, X. et al. Metal-containing carbon nitride compounds: a new functional organic–metal hybrid material. *Adv. Mater.* **21**, 1609–1612 (2009).
24. Li, Y. et al. Implementing metal-to-ligand charge transfer in organic semiconductor for improved visible-near-infrared photocatalysis. *Adv. Mater.* **28**, 6959–6965 (2016).

25. Gao, G., Jiao, Y., Waclawik, E. R. & Du, A. Single atom (Pd/Pt) supported on graphitic carbon nitride as an efficient photocatalyst for visible-light reduction of carbon dioxide. *J. Am. Chem. Soc.* **138**, 6292–6297 (2016).
26. Huang, P. et al. Selective CO_2 reduction catalyzed by single cobalt sites on carbon nitride under visible-light irradiation. *J. Am. Chem. Soc.* **140**, 16042–16047 (2018).
27. Thomas, A. et al. Graphitic carbon nitride materials: variation of structure and morphology and their use as metal-free catalysts. *J. Mater. Chem.* **18**, 4893–4908 (2008).
28. Zhang, Z. et al. High-pressure bulk synthesis of crystalline $C_6N_9H_3{\cdot}HCl$: a novel C_3N_4 graphitic derivative. *J. Am. Chem. Soc.* **123**, 7788–7796 (2001).
29. Wirnhier, E. et al. Poly(triazine imide) with intercalation of lithium and chloride ions $[(C_3N_3)_2(NH_xLi_{1-x})_3{\cdot}LiCl]$: a crystalline 2D carbon nitride network. *Chem. Eur. J.* **17**, 3213–3221 (2011).
30. Algara-Siller, G. et al. Triazine-based graphitic carbon nitride: a two-dimensional semiconductor. *Angew. Chem. Int. Ed.* **53**, 7450–7455 (2014).
31. Lin, L., Yu, Z. & Wang, X. Crystalline carbon nitride semiconductors for photocatalytic water splitting. *Angew. Chem. Int. Ed.* **58**, 6164–6175 (2019).
32. Bojdys, M. J., Müller, J.-O., Antonietti, M. & Thomas, A. Ionothermal synthesis of crystalline, condensed, graphitic carbon nitride. *Chem. Eur. J.* **14**, 8177–8182 (2008).
33. Lin, L. et al. Photocatalytic overall water splitting by conjugated semiconductors with crystalline poly(triazine imide) frameworks. *Chem. Sci.* **8**, 5506–5511 (2017).
34. Lin, L., Ou, H., Zhang, Y. & Wang, X. Tri-*s*-triazine-based crystalline graphitic carbon nitrides for highly efficient hydrogen evolution photocatalysis. *ACS Catal.* **6**, 3921–3931 (2016).
35. Waddell, E. M. & Chapman, J. N. Linear imaging of strong phase objects using asymmetrical detectors in STEM. *OPTIK* **54**, 83–96 (1979).
36. Lazić, I., Bosch, E. G. T. & Lazar, S. Phase contrast STEM for thin samples: integrated differential phase contrast. *Ultramicroscopy* **160**, 265–280 (2016).
37. Chong, S. Y. et al. Tuning of gallery heights in a crystalline 2D carbon nitride network. *J. Mater. Chem. A* **1**, 1102–1107 (2013).
38. Ham, Y. et al. Synthesis and photocatalytic activity of poly(triazine imide). *Chem. Asian J.* **8**, 218–224 (2013).
39. Kang, Y. et al. Selective breaking of hydrogen bonds of layered carbon nitride for visible light photocatalysis. *Adv. Mater.* **28**, 6471–6477 (2016).
40. Li, X. et al. $CsPbX_3$ quantum dots for lighting and displays: room-temperature synthesis, photoluminescence superiorities, underlying origins and white light-emitting diodes. *Adv. Funct. Mater.* **26**, 2435–2445 (2016).
41. Sun, S. et al. The origin of high efficiency in low-temperature solution-processable bilayer organometal halide hybrid solar cells. *Energy Environ. Sci.* **7**, 399–407 (2014).
42. Cao, Y. et al. Improved quantum efficiency for electroluminescence in semiconducting polymers. *Nature* **397**, 414–417 (1999).
43. Kippelen, B. & Brédas, J.-L. Organic photovoltaics. *Energy Environ. Sci.* **2**, 251–261 (2009).
44. Brédas, J.-L., Norton, J. E., Cornil, J. & Coropceanu, V. Molecular understanding of organic solar cells: the challenges. *Acc. Chem. Res.* **42**, 1691–1699 (2009).
45. Li, G., Chang, W.-H. & Yang, Y. Low-bandgap conjugated polymers enabling solution-processable tandem solar cells. *Nat. Rev. Mater.* **2**, 17043 (2017).
46. Kattel, S., Liu, P. & Chen, J. G. Tuning selectivity of CO_2 hydrogenation reactions at the metal/oxide interface. *J. Am. Chem. Soc.* **139**, 9739–9754 (2017).
47. Wang, D., Liu, Z.-P. & Yang, W.-M. Revealing the size effect of platinum cocatalyst for photocatalytic hydrogen evolution on TiO_2 support: a DFT study. *ACS Catal.* **8**, 7270–7278 (2018).
48. Chen, J. S. et al. Constructing hierarchical spheres from large ultrathin anatase TiO_2 nanosheets with nearly 100% exposed (001) facets for fast reversible lithium storage. *J. Am. Chem. Soc.* **132**, 6124–6130 (2010).
49. Maeda, K. et al. Noble-metal/Cr_2O_3 core/shell nanoparticles as a cocatalyst for photocatalytic overall water splitting. *Angew. Chem.* **118**, 7970–7973 (2006).
50. Shen, B. et al. Atomic spatial and temporal imaging of local structures and light elements inside zeolite frameworks. *Adv. Mater.* **32**, 1906103 (2020).
51. Kirkland, E. J. *Advanced Computing in Electron Microscopy* (Springer Science and Business Media, 2010).
52. Kresse, G. & Furthmüller, J. Efficient iterative schemes for ab initio total-energy calculations using a plane-wave basis set. *Phys. Rev. B* **54**, 11169–11186 (1996).
53. Kresse, G. & Furthmüller, J. Efficiency of ab-initio total energy calculations for metals and semiconductors using a plane-wave basis set. *Comput. Mater. Sci.* **6**, 15–50 (1996).
54. Blöchl, P. E. Projector augmented-wave method. *Phys. Rev. B* **50**, 17953–17979 (1994).
55. Kresse, G. & Joubert, D. From ultrasoft pseudopotentials to the projector augmented-wave method. *Phys. Rev. B* **59**, 1758–1775 (1999).
56. Perdew, J. P., Burke, K. & Ernzerhof, M. Generalized gradient approximation made simple. *Phys. Rev. Lett.* **77**, 3865–3868 (1996).
57. Grimme, S. Semiempirical GGA-type density functional constructed with a long-range dispersion correction. *J. Comput. Chem.* **27**, 1787–1799 (2006).
58. Monkhorst, H. J. & Pack, J. D. Special points for Brillouin-zone integrations. *Phys. Rev. B* **13**, 5188–5192 (1976).

Acknowledgements

This work was financially supported by the National Key R&D Program of China (2018YFA0209301), the National Natural Science Foundation of China (U1905214, 21961142019, 21425309, 21761132002, 21861130353, 21802021, 21973014, 51701170 and 51871058), the Chang Jiang Scholars Program of China (T2016147), the project of science and technology plan of Fujian Province (2018J01520) and the 111 Project (D16008). This work made use of the TEM resources at Fuzhou University and the Nanoport Europe of Thermo Fisher Scientific in the Netherlands. Z. Yu thanks A. Carlsson for professional assistance in iDPC imaging.

Author contributions

X.W. conceived and designed the experiment. L.L., Z.L. and J.Z. synthesized the experimental samples and carried out most of the characterization, as well as the photocatalytic reactions. Z.L. and Z.Y. performed the SEM and TEM characterizations. Z.Y. analysed the TEM data. X.C. and W.L. carried out the DFT calculations. X.W. supervised the experiments. All the authors discussed the results and wrote the manuscript.

Competing interests

The authors declare no competing interests.

Additional information

Supplementary information is available for this paper at https://doi.org/10.1038/s41929-020-0476-3.

Correspondence and requests for materials should be addressed to X.W.

Reprints and permissions information is available at www.nature.com/reprints.

Publisher's note Springer Nature remains neutral with regard to jurisdictional claims in published maps and institutional affiliations.